Experimental study of the shear strength of a snow-mortar interface

Experimental study of the shear strength of a snow-mortar interface

Gianmarco Vallero[a,*], Monica Barbero[a], Fabrizio Barpi[a], Mauro Borri-Brunetto[a], Valerio De Biagi[a], Yoichi Ito[b], and Satoru Yamaguchi[b]

[a] Department of Structural, Building and Geotechnical Engineering (DISEG Department), Politecnico di Torino, c.so Duca degli Abruzzi 24, 10129 Turin (Italy)

[b] Snow and Ice Research Center, National Research Institute for Earth Science and Disaster Resilience (NIED), Suyoshi, Nagaoka, Niigata, 940-0821 Japan

* Correspondence to: gianmarco.vallero@polito.it

Author abbreviations: gianmarco.vallero@polito.it (G.V.); monica.barbero@polito.it (M.B.); fabrizio.barpi@polito.it (F.B.); mauro.borri@polito.it (M.B.B.); valerio.debiagi@polito.it (V.D.B.); y_ito@bosai.go.jp (Y.I.); yamasan@bosai.go.jp (S.Y.)

Abstract: Within the wide field of snow mechanics the shear strength of snow is paramount. In the scientific literature a wide number of experimental and theoretical works exist with reference to the progressive shear failure of snow-snow interfaces under different conditions of internal and external actions. On the contrary, to our knowledge, few studies are devoted to the shear behaviour at the contact between a snow layer and a solid stiff material, although this topic could have various fields of application (e.g., glide avalanches, snow removal, snow-structure interaction, etc.). Here, we analyze results of experimental direct shear tests carried out in displacement control on a snow-mortar interface at given conditions of temperature and sintering times. We additionally use the Mohr-Coulomb failure criterion to represent shear strength along the interface both in failure and post-failure conditions.

Keywords: snow mechanics; snow friction; shear test; shear failure; Mohr-Coulomb criterion

1 Introduction

The shear strength and the related frictional behaviour of snow layers are topics of broad interest, both in the field of Civil and Environmental Engineering, with particular application to the field of snow avalanche forecasting and hazard assessment. Historically, such applications have been extensively studied (e.g., Casassa et al., 1991, 1989; Conway and Abrahamson., 1984; Gauthier et al., 2010; Gleason, 2002; McClung, 1977; Mellor, 1975). For instance, the shear strength of snow weak layers is fundamental to researchers' studies devoted to slab avalanche release and their triggering mechanisms (McClung, 1979; Mede et al., 2018; Podolskiy et al., 2014; Schweizer et al., 2003). Several of these authors have used experimental methods and have introduced devices specifically designed to perform direct and simple shear tests on snow samples mainly for understanding avalanche triggering mechanisms. For instance, Reiweger et al. (2009) designed a load-controlled apparatus to perform tilt tests on homogeneous and layered snow samples in a cold laboratory under

controlled conditions. Matsushita et al. (2012) developed a simple shear frame for assessing the influence of temperature and normal load in the shear resistance of artificial snow. Finally, Barbero et al. (2016) introduced a portable apparatus which was able to carry out direct shear tests on snow samples directly on-site. This latter device was used by De Biagi et al. (2019) to perform cold laboratory tests on reconstructed snow samples with artificial faceted snow layers.

Despite these studies on snow interfaces and shear strength, limited research can be found regarding the shear behaviour of a snow layer deposited onto a stiff material, e.g., rock or concrete. In general, some authors suggested that frictional behaviour of snow in contact with other materials could be investigated using ice instead of snow (Colbeck, 1994; Jellinek, 1960; Kietzig et al., 2010). This choice seems to be related to the greater repeatability of the mechanical properties that can be attained for a laboratory ice sample compared to those for a snow one. As a result, many problems concerning snow contact are faced with reference to ice, particularly in the field of winter sports and leisure activities (Kietzig et al., 2009). To our knowledge, only a few researchers have provided further indications on the shear behaviour at the snow-stiff solid material interface. For instance, Inoue and Honda (1955) carried out a series of contact tests on snow-solid interfaces using two different materials (glass and polytetrafluoroethylene). Their results show that snow adheres to the underneath material and this adhesion is dependent on the presence of a liquid water film at the interface. Inoue and Honda (1955) attempt to quantify the adhesion strength using the equivalent angle though no concrete conclusions could be drawn due to the limitations of the experimental device. Mellor (1975) provided a review of snow mechanics which included general information regarding snow adhesion and frictional behaviour in contact with solids. For example, he stated that the bond strength usually increases with decreasing temperature and varies with the surface properties of the solid material (i.e., roughness, hydrophobicity, etc.). More recently, McCallum (2014) examined friction between a stainless steel cone and polar snow, using the Mohr-Coulomb criterion, to interpret the results of CPT tests and quantify the compressive strength of snow. Heil et al. (2020) quantitatively measured the shear adhesion strength and surface energy of snow layer deposited on several solid surfaces (AL 6061, HDPE, stainless steel, and copper) with a non-destructive apparatus that accounted for the liquid water content at the interface. Jelle (2013) studied the problem of snow removal from photovoltaic modules and performed several experiments to determine the static and dynamic friction coefficients between snow and various roofing materials (glass, steel, bricks, polymers, concrete, and

60 bitumen). These tests were carried out using both a tension machine and a tailor-made friction table where the
61 slip angle could be easily determined. The results show that during friction experiments snow slabs froze on
62 the substrate surface because of the formation of adhesive forces (i.e., electromagnetic or electrostatic forces),
63 which are strong enough even at inclination angles of about 90 degrees. Finally, Bartko and Baskaran (2018)
64 investigated the problem of snow redistribution between building roofs by carrying out experimental tests
65 using different commercial roofing materials.

66 This topic has many other applications, such as in the framework of glide avalanche release and evolution,
67 the assessment of the basal friction and its reduction related to local failures of the snow-ground interface or
68 to the presence of water films and moisture (Ancey and Bain, 2015; Mitterer and Schweizer, 2012; Puzrin et
69 al., 2019). Another possible application is represented by slopes subjected to shallow landslides and reinforced
70 by the application of shotcrete: when a slope with shotcrete reinforcement is covered by an intense snowfall,
71 a snow avalanche can be triggered. Moreover, the comprehension of the shear mechanisms at the snow-solid
72 material interface can aid some engineering problems such as that of thick snow slabs deposited on civil
73 structures and infrastructures (roofs, walls, tunnels, bridges, etc.) or upon roads. In this latter case, the
74 compaction of snow made by vehicles could influence the friction of the snow on the underlying road surface
75 compromising traveler safety (Abele, 1963; Shapiro et al., 1997). Also, understanding snow-solid surface
76 friction is critical for defining the power required for snowploughs or the effects of compaction of tyres on
77 roads and airport runways (McCallum and White, 2016). Finally, especially in arctic environments, the design,
78 construction and maintenance of snow runways need a better knowledge of this topic (White and McCallum,
79 2018).

80 In this paper, we try to address this gap in knowledge by presenting the results of an experimental campaign
81 carried out on 36 interface specimens made of a snow layer deposited and sintered over a cementitious mortar
82 slab. Mortar was chosen as the stiff substrate because it possesses typical features of construction materials
83 and, at the same time, some characteristics of natural materials (e.g., rock). The activity was performed with
84 the portable direct shear test apparatus described by Barbero et al. (2016), modified in order to conduct tests
85 in displacement-controlled mode (De Biagi et al., 2019a). Two sintering times and two testing temperatures
86 were used in order to study their influence on the shear strength of the interface. The testing conditions were

87 varied to reproduce conditions that could be potentially obtained on-site (e.g., temperatures, vertical loads,
88 sintering and isothermal metamorphisms).

89 2 Materials and methods

90 The direct shear tests on snow-mortar interfaces were carried out in the framework of a scientific
91 collaboration between Politecnico di Torino (Torino, Italy), and the Snow and Ice Research Center of the
92 National Research Institute for Earth Science and Disaster Resilience, NIED (Nagaoka, Japan). The
93 experimental activity was carried out in February 2019 in the cold laboratories of NIED (Nagaoka, Japan) at
94 controlled conditions of temperature. All the experiments were performed with a displacement-controlled
95 portable device for direct-shear tests, which is capable of applying adjustable normal pressure and
96 displacement rates as previously developed by some of the authors (Barbero et al., 2016).

97 *2.1 The direct-shear test apparatus*

98 The test apparatus consists of a series of tools that can carry out direct shear tests without external aids (i.e.,
99 no public electric power, pressurized-air system, etc.). This system was previously developed by Barbero et
100 al. (2016) for on-site measurements of the mechanical characteristics of weak snow layers in avalanche release
101 zones. The relatively small weight of the device (about 7 kg) and its compact power supply and control unit
102 allow its operation in remote mountainous areas. In addition to this, the apparatus can be used to perform
103 experimental activity in equipped laboratories such as in the case presented here.

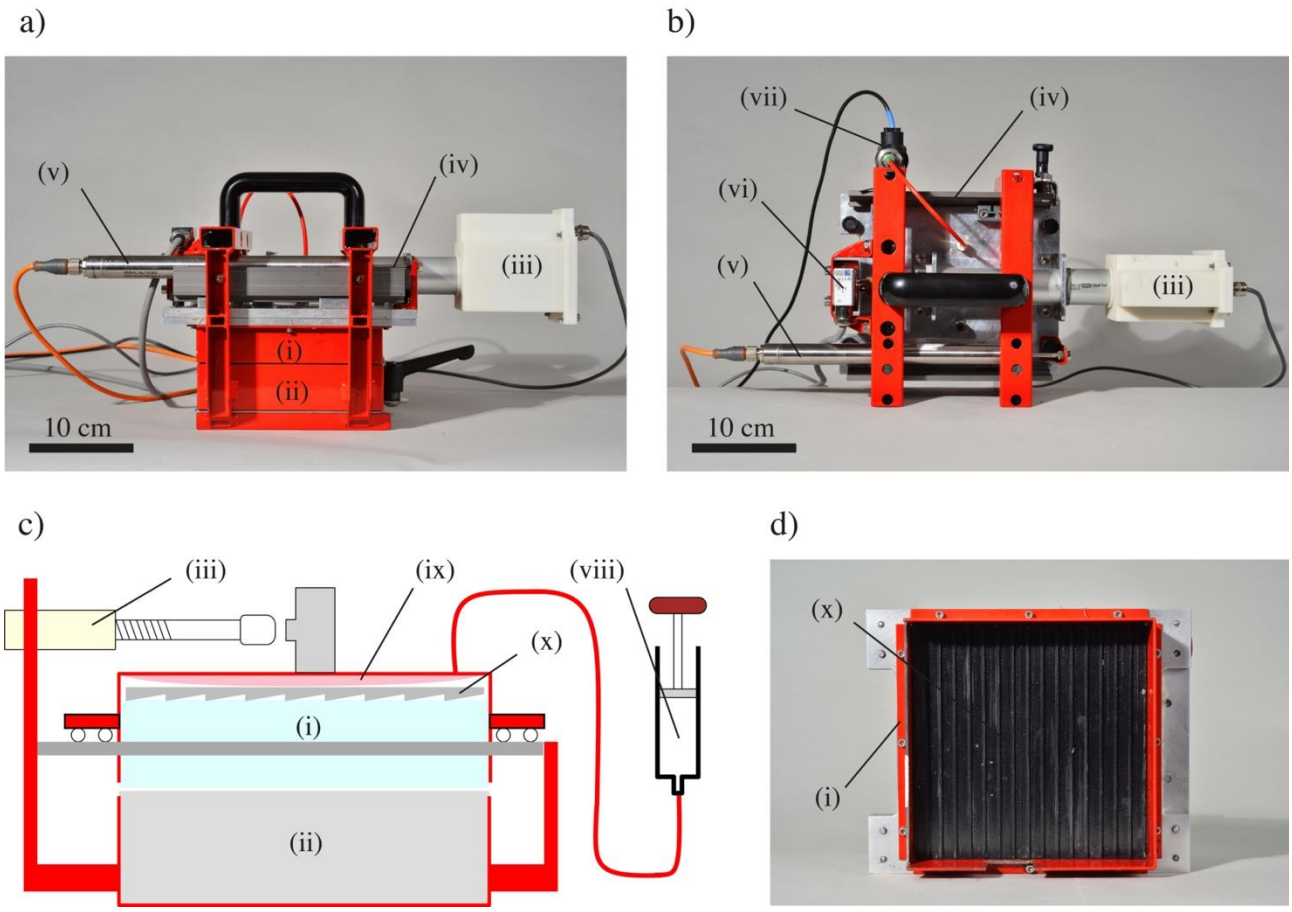

Figure 1 a) and b) Lateral and top views of the testing device (shear box): (i) upper moving drawer (with upper part of the specimen), (ii) lower fixed drawer (with lower part of the specimen), (iii) stepper motor, (iv) sliding guides, (v) LVDT, (vi) load transducer, (vii) pressure transducer. The control system, (data logger) and the air portable reservoir are not shown; c) Sketch of the testing device cross section: nos. from (i) to (vii) are equal to the ones in sub-figures a) and b), viii) external air reservoir, ix) inner air chamber, x) top cap of the moving drawer; d) Bottom view of the moving drawer in which is clearly visible the saw-tooth surface of the top cap.

The main device of the apparatus is the "shear box" consisting of a steel frame (Figures 1a, 1b, and 1c) with a lower fixed and upper moving drawer. The inner part is empty and is able to host a specimen having dimensions 160 mm × 160 mm × 72 mm (length × width × height). Thus, the area subjected to shear stress is equal to 256 cm^2.

The lateral displacement, i.e., the shear displacement, is applied by a linear electric actuator with a motor controlled by an electric drive. The normal operational displacement rates are in the range of 1-100 mm min^{-1}. The motion is constrained by a couple of linear guides made of hard-anodized aluminum (Igus DryLin WSQ-10) with plastic low-friction sliding bearings, held by chromate zinc die-cast supports.

120 The normal stress on the interface is applied through the inflation of a rubber square-shaped membrane in
121 the higher part of the upper drawer (Figure 1c). A polymeric cap with saw-tooth surface (called "top cap",
122 hereafter), glued to the membrane, was installed in order to improve the transmission of the shear force applied
123 during the test to the snow layer (Figure 1d). The membrane was pressurized through an external portable and
124 manual control air reservoir, i.e., a gardener pump, with volume of 5 dm^3 and maximum pressure of 3 bars. A
125 rectangular window (50 mm × 30 mm) is located on the side wall of the device allowing to directly observe
126 the displacement field in the upper and lower part of the sample (De Biagi et al., 2019b).

127 During the execution of the tests, the apparatus measures the pressure in the air chamber, the relative
128 displacements between the upper and lower part of the shear box, and the horizontal shear force by using a
129 pressure gauge, a linear variable displacement transducer (LVDT) and a load transducer, respectively. A
130 sampling rate of 2 kHz was adopted for all the acquired measures. The apparatus is interfaced through a
131 National Instruments CompactDAQ control and acquisition unit, to a PC running a LabVIEW program, to
132 control the testing parameters and to record all the experimental data over time.

133 *2.2 Snow-mortar samples*

134 The experimental tests were performed on artificially made samples consisting of two superimposed slabs
135 (Figure 2a). The two different parts are briefly described in the following:

136 - the lower part is a square prism (160 × 160 × 40 mm^3) made of cementitious mortar.
137 - the upper part is a square prism (160 × 160 × 32 mm^3) made of artificially reconstituted snow.

138 In the following, the main phases of the specimen preparation are reported: all the phases were carried out
139 in the NIED cold rooms and, at the end of the process, a snow-mortar interface specimen was ready for the
140 execution of the direct shear test.

141 1. The snow was harvested outside the NIED laboratories and stored in the cold rooms of the research
142 center (at a temperature of -10 °C) until the execution of the tests.
143 2. The mortar slab is placed on a table.
144 3. A two-part transparent mold is positioned around the mortar slab.
145 4. The snow was sieved to select only the grains with maximum size between 0.7 and 1.0 mm (Figure
146 2b) and then immediately poured into the mold, over the mortar slab.

5. The height of the snow layer is kept higher than the final target (i.e., > 32 mm).
6. A vertical 100 N load is applied to the sample over a short period t_c = 5 minutes (compaction phase, see Figure 3).
7. After the compaction the load is removed.
8. The mortar-snow specimen is left in the mold for the required sintering time t_s under isothermal conditions (sintering phase, see Section 2.3).
9. The upper part of the mold is removed.
10. The upper part of the snow sample was removed to reduce the height of the snow layer to the required value (i.e., 32 mm).
11. The bottom part of the mold is removed, and the snow-mortar sample is ready for the execution of the test.

The grain size was chosen to represent the typical dimension of sintered hard slab snow that can be observed in nature (McClung and Schaerer, 2006). The final snow density was between 430 and 460 kg m^{-3}. At the grain scale, the sintering process generated clearly visible necks (Figure 2b). Thus, according to the international morphological classification of seasonal snow (Fierz et al., 2009), the snow is identified as RG-lr. It should be noted that, in this work, the expression "sintering time" defines the time period (t_s) experienced by each sample during which the isothermal sintering process (i.e., the creation and growth of bonds among grains) takes place. The snow hardness was measured using a push-pull gauge (model RZ-10, Aikoh Engineering) (Sugiura et al., 2011; Takeuchi et al., 1998).

A total number of nine mortar slabs were used to optimize the production of the specimens and the timing of the experimental activity. The characteristics of the snow and of the mortar are summarized in Table 1.

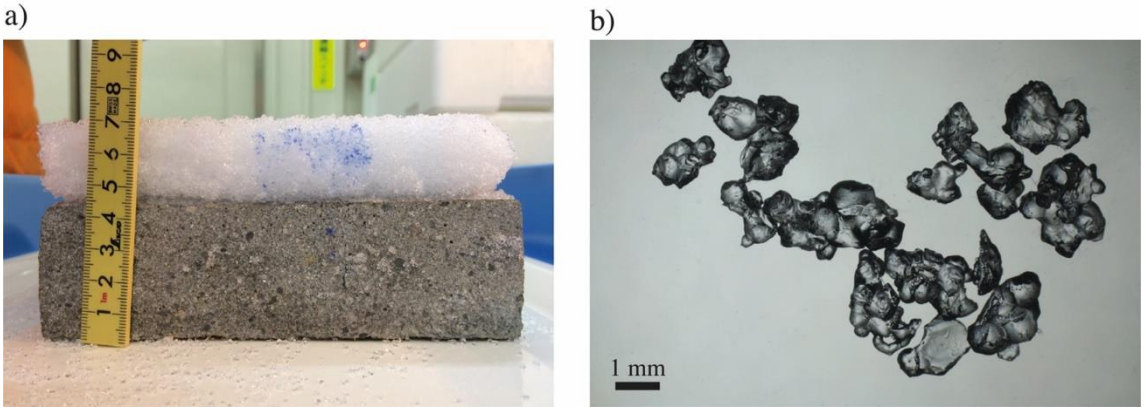

Figure 2 a) Example of a snow-mortar interface specimen; b) Micro-photo of the grains composing the upper half of the specimen. It can be clearly seen that single grains are connected by necks generated by snow metamorphism.

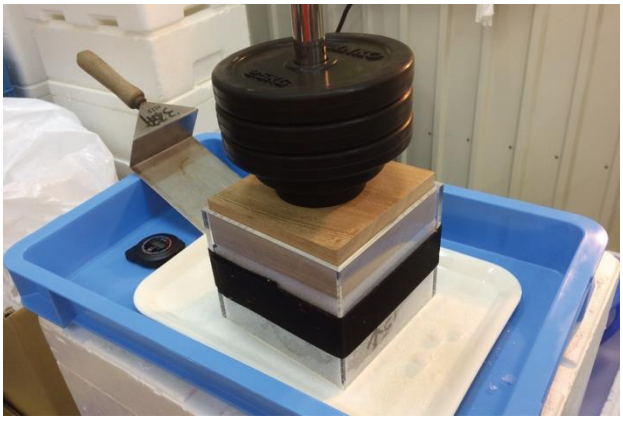

Figure 3 Compaction phase of the interface specimen under vertical load (100 N). The mold is of a prismatic shape with dimensions of (160 × 160 mm^2) and is used for the snow specimens. The weight is set to impose a uniform and repeatable initial condition.

Table 1 Geometrical and physical characteristics of the different parts of the snow-mortar interface specimens. The heights of the two parts of the specimen are mean values and some variations can be observed among samples. More details for the hardness can be found in Sect. 2.3.

	Snow	Mortar
Density	445 ± 9 kg m^{-3} (95%)	2 200 kg m^{-3}
Snow Type	RG-lr	-
Snow grain size	0.7 – 1.0 mm	-
Snow hardness	One finger (1F), Four fingers (4F)	-
Basal area	Square, 160 × 160 mm^2	Square, 160 × 160 mm^2
Height	32 mm	40 mm

180 *2.3 Tests*

181 The entire experimental activity was devoted to understanding the influence of both sintering time and
182 temperature on the strength of snow-mortar interfaces. Thus, four combinations of different sintering times
183 and temperatures were introduced, defining four groups of specimens code-named LS-T1, LS-T2, SS-T1, and
184 SS-T2. LS and SS stand for long and short sintering time conditions, respectively, while T1 and T2 indicate
185 the test temperatures of −10 °C and −5 °C, respectively. All samples were subjected to an initial compaction
186 phase (t_c = 5 minutes) under a vertical compressive load of about 100 N (producing a vertical stress 3.9 kPa)
187 in order to generate a denser snow layer simulating dry hard snow slabs. Then, SS samples were obtained after
188 a following sintering time (t_s) shorter than 20 minutes, while, for LS samples, t_s was longer than 20 hours.

189 It can be observed that for LS-T1 and LS-T2 specimens the average hardness was 26.4 kPa and 16.9 kPa,
190 respectively (see Table 1). These values were obtained with the micro-penetrometer and are comparable with
191 the one-finger limit (1F) defined by the classical hand test (Höller and Fromm, 2010). SS-T1 and SS-T2 were
192 tested with the same procedure, obtaining the average hardness values of 4.6 kPa and 4.1 kPa, both comparable
193 to four fingers hardness (4F). This observation confirms that the specimen preparation procedure permits
194 obtaining samples of different hardness depending on the sintering time and on the storage temperature.

195 In order to investigate the influence of the normal stress on the interface shear strength, three levels of
196 normal stress were adopted: Low-Pressure (LP = 5.0 kPa), Medium-Pressure (MP = 7.5 kPa), and High-
197 Pressure (HP = 10.0 kPa). These values were chosen to take into account the effects of different thicknesses
198 of the snowpack that can potentially cover the interface. For instance, considering a snow density of 450 kg
199 m^{-3}, the three levels LP, MP and HP are related to snowpack heights of 1.1 m, 1.7 m and 2.3 m, respectively.
200 Three tests for each sintering, temperature and pressure combination were performed for a total number of 36
201 direct shear tests.

202 Unfortunately, it was not possible to keep constant the normal stress during the execution of the test. This
203 is due to several peculiarities of the shear apparatus:

204 1. The normal stress is applied by means of an inflated rubber membrane by using a portable hand-
205 driven air pump that has to be controlled by an operator during the test. This method was adopted

because the shear apparatus is designed to perform on-site direct shear tests that have to be performed rapidly and with a light equipment;

2. The volume of the inflated rubber membrane is reduced. Thus, a small variation in its volume, due for example to rotations of the top snow surface, can cause a substantial variation of the air pressure transmitted to the snow-mortar sample.

Therefore, it is not possible to relate a unique value of the normal stress to each test as typically should occur during an ideal shear test in which the normal stress remains constant. Here, in comparison to other studies, the continuous monitoring and measurement of the air pressure in the membrane, and a careful and appropriate choice of the normal stress values to be used during the phase of result interpretation are necessary.

The main conditions characterizing the shear tests are reported in Table 2. The two testing temperatures were chosen to represent two different conditions of the snow, according to the available cold rooms of the NIED laboratory. Higher temperatures, near to 0 °C, that could be representative of a more realistic soil-snow interface were discarded in order to preserve the integrity of the snow part of the specimens from melting during the execution of the tests. The adopted displacement rate and maximum shear displacement had fixed values equal to 10 mm min^{-1} and 20 mm, respectively. Particularly, these values were chosen to: i) take into account a mean shear rate among the ones usually used in many literature examples in which the mechanical behaviour of snow is studied (Matsushita et al., 2012; McClung, 1977; Puzrin et al., 2019; Reiweger et al., 2010), ii) catch and distinguish all loading, rupture and irreversible sliding phenomena occurring at the snow-mortar contact, and iii) neglect some undesired dynamic effects that can potentially compromise measurements. During the experimental activity the effect of velocity (i.e., displacement rate) was not investigated because the displacement rate was not changed.

Table 2 Environmental and testing conditions during the experimental campaign.

Parameter	Value
Cold room temperature (T1, T2)	T1 = -10 °C, T2 = -5 °C
Maximum shear displacement range (u_{max})	20 mm
Shear displacement rate ($\dot{u}$)	10 mm min^{-1}
Average test time (t)	120 s

To document the progressive failure of the interfaces, the specimen was filmed during the test through the window located on the external side of the shear box with a high-speed video camera (Sony RX10-IV, 24-600 mm lens) operating at 30 fps (RGB, 3840 × 2160 pixels). The sensor was located at 290 ± 5.5 mm from the sample surface and its plane was kept parallel to the lateral side of the target. Moreover, a lamp was used in order to obtain well defined videos. To enhance the contrast of the natural pattern of the snow sample surface, a blue nebulized ink was sprayed within the shear box window. Starting from these videos, each frame was extracted and stored as a black and white TIFF image file. Because it was not possible to trigger automatically both camera and testing apparatus, the synchronization of the video recordings with the physical measurements was obtained by comparing the displacement fields observed on the video frames and the ones measured through the LVDT. The beginning of the displacement in the video recording was determined by tracking marker points located on the shear box frame with the Digital Image Correlation technique (DIC, hereafter) implemented in the open source tool DICe (Turner et al., 2015). When the horizontal displacement measured with the DIC technique deviated from the null value, the corresponding frame was related to the same displacement value recorded by the LVTD.

2.4 Preliminary data processing

The data (i.e., the "raw data", hereafter) collected by the sensors underwent a correction procedure prior to analysis and interpretation. Besides the variability of the normal stresses, raw data are indeed considerably disturbed by other causes such as the electric-induced noise (related to the thermal motion of charges in electric circuits) and the random white noise affecting all the sensors output. The former is mainly related to the service frequency of the Japanese electric power distribution (i.e., 50 Hz, according to the Eastern Japanese standard) while the latter is generally due to the nominal measure range of the gauges. For instance, the pressure transducer has a range of measure from 0 to 50 kPa which is wider than the measured quantities (having a maximum of 10 kPa), so that the noise in pressure data is more evident than that existing in the other measured quantities (e.g., the displacement). Furthermore, another set of corrections is needed to consider the calibration of the quantities measured by the shear test system (i.e., the sliding guides friction, the air-pressure/normal-stress relation, and the progressive reduction of the contact area). The following data correction steps were employed:

1. Download of the raw data arrays (i.e., test time *t*, shear displacement *u*, air pressure *p*, and shear force *T*) from the acquisition/control system. The sampling rate is the same for every array (i.e., f_0 = 2 kHz). An example of the original raw data collected by the transducers is presented in Figure 4a.
2. Execution of the Short-Time Fourier Transform (STFT) (Portnoff, 1980) and the following Low-Pass Filter (50 Hz threshold) on the raw data to remove the electric-induced noise. Then, a moving average of the data, with a computational window width of 0.25 s, was carried out to reduce the residual white noise. Resampled data obtained via this procedure were used in the following operations.
3. Computation of the corrected normal stress σ_c starting from the air pressure p:

$$\sigma_c = \frac{kp}{R} \tag{1}$$

where: $k = 0.797$ is a coefficient, experimentally determined, which relates the imposed pressure in the air chamber *p* to the normal stress σ_c acting on the sample in the initial conditions of zero shear displacement and takes into account the incomplete contact and friction; $R = \frac{A_c}{A_n} = 1 - \frac{u}{d}$ is the ratio between the reduced contact area A_c, for a certain lateral displacement *u*, and the nominal area $A_n = d^2$, and $d = 160$ mm is the length of the lateral side of the square sample.

4. Evaluation of the friction force T_g, acting on the sliding guides, which reduces the actual shear load transmitted to the specimen. The following equation (determined experimentally) was used:

$$T_g = \mu_d N_c + T_0 \tag{2}$$

where N_c is the corrected normal force defined as $N_c = \sigma_c A_c$, $\mu_d = 0.053$ is the dynamic friction coefficient and $T_0 = 1.373$ N. The friction force is, in general, influenced by the displacement rate, which has been set to 10 mm min^{-1} in all the tests presented here.

5. Determination of the corrected shear stress τ_c with the following relation:

$$\tau_c = \frac{T - T_g}{A_c} = \frac{T - T_g}{RA_n} \tag{3}$$

in which *T* is the shear force measured by the load transducer.

6. Re-sampling operation (with a frequency $f_1 = 40$ Hz) of the corrected data to reduce the computational effort and the size of the output files without loss of information.

In Figure 4b, the corrected data referred to the LS-T1 test no. 1 are reported. All the above-described steps were performed on each test in order to obtain a corrected set of data. The cleaning operation was performed on all the sensor raw data, while the correction formulae in Eqns. (1) and (3) were implemented only for normal and shear stresses. In practice, applying Eqns. (1) and (3) to raw data means deforming their graphs in some way: during the first part of the test, the applied corrections reduce the normal and shear stress values while the contrary happens in the second part. This is due to the progressive reduction of the contact area, related to the nature of the considered tests.

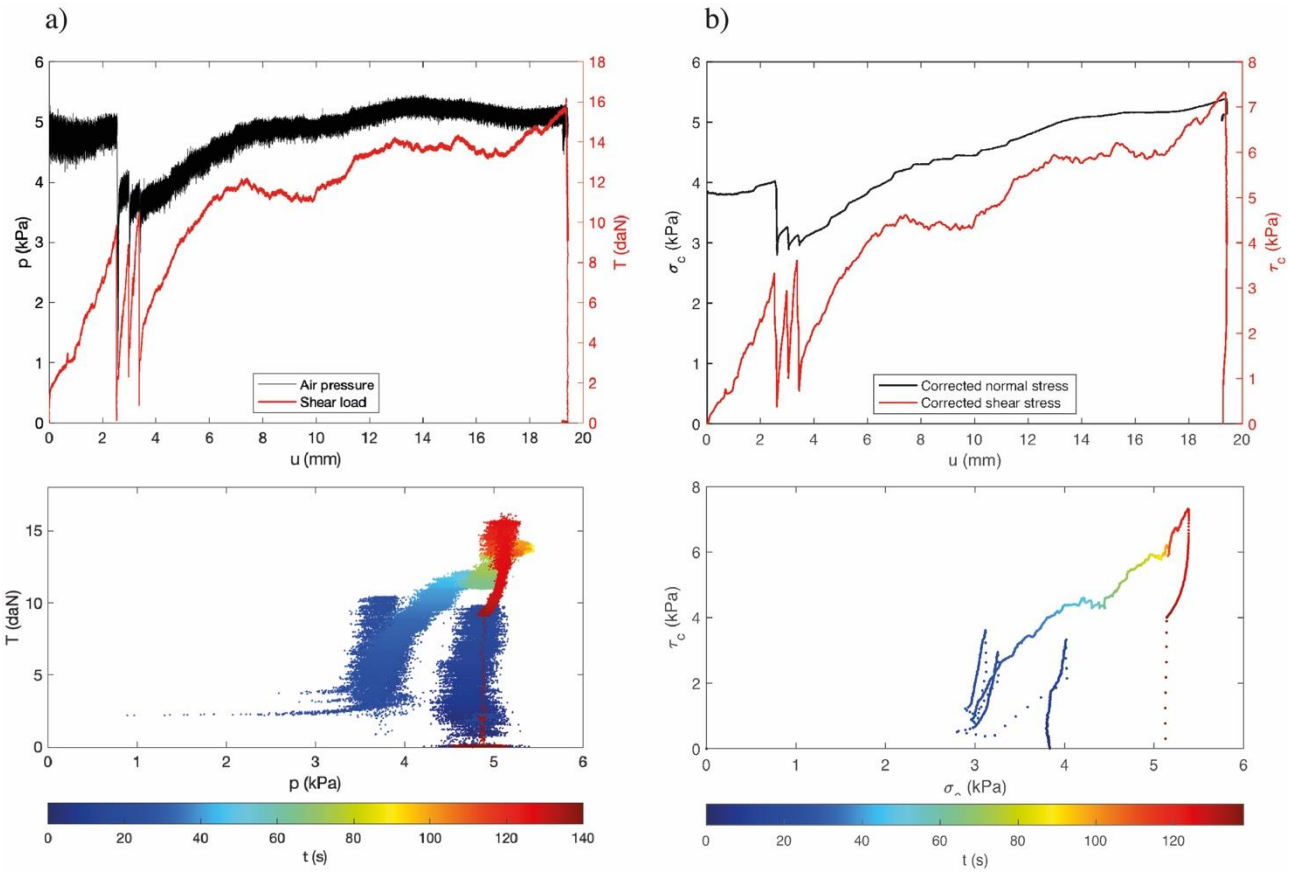

Figure 4 Comparison between raw and corrected data with reference to test LS-T1 no. 1: a) Raw data recorded by the acquisitions system. In the upper plots, it can be seen the considerable variability and the random noise that affect the pressure signal. In the lower graphs the same data are plotted in the $\sigma - \tau$ plane with a colormap highlighting the evolution in time of the data; b) Corrected data obtained by the application of Eqn. (1) and (3).

3 Results

3.1 Generality

The results of a typical snow-mortar direct shear test are shown in Figure 5 with reference to LS-T1 test no. 1 and its shear stress evolution in time. In almost all tests, two processes can be clearly observed: i) an initial *loading process*, and ii) a following macroscopic *sliding process*. Similar curves can be found in literature for stainless steel-snow shear strength (McCallum and Wiegand, 2018). During the former process, the horizontal applied load was gradually transferred to the snow-mortar interface until the detachment of the snow layer from the mortar slab occurs. The progressive damage of the snow-mortar interface is a complex phenomenon that involves the whole loading process. In this work, the *interface failure* (Figure 5) is defined as the definitive instantaneous rupture of the snow-mortar surface bonds that promotes the detachment of the snow layer from the underneath mortar slab and the beginning of the irreversible macroscopic sliding. In the loading process a certain number of peaks can be clearly observed in $\tau - t$ graphs (Figure 5) that can be related to local rupture of the snow-mortar surface. Then, during the second process (i.e., the sliding one), the snow half of the sample macroscopically slides over the mortar slab and the relative shear displacement develops irreversibly until the maximum displacement $u_{max} = 20$ mm is reached (i.e., the end of the test).

Referring to the loading process, each shear stress peak was followed by an instantaneous drop of both shear and normal stresses. Typically, the last one was related to the failure of the interface (i.e., the detachment of the snow layer from the mortar block). In 90% of cases, samples failed before reaching a displacement of 4.80 mm (median value: 2.84 mm, mean value: 2.89 mm, standard deviation: 1.88 mm). More details can be found in Table 3 by considering separately the four classes of specimens. With reference to the average standard deviation values, all the LS specimens (i.e., both LS-T1 and LS-T2) and the SS-T2 ones seem to be less scattered than the SS-T1 samples. From test video recordings, it is observed that SS-T1 specimens are the least bonded, as they have undergone the shorter sintering time and have been subjected to the lower temperature. Both these aspects (shorter sintering time and lower temperature) can justify the behaviour of the SS-T1 group of tests, the great variability that characterizes their results, and the large value of the standard deviation. SS specimens (i.e., both SS-T1 and SS-T2) generally reached larger displacements before failing. Otherwise, LS specimens failed before the SS ones, for both temperatures, and show less variability in the

results. In fact, LS specimens were the hardest ones and once failed they behaved very similarly to a hard snow slab sliding rigidly over the stiff substrate.

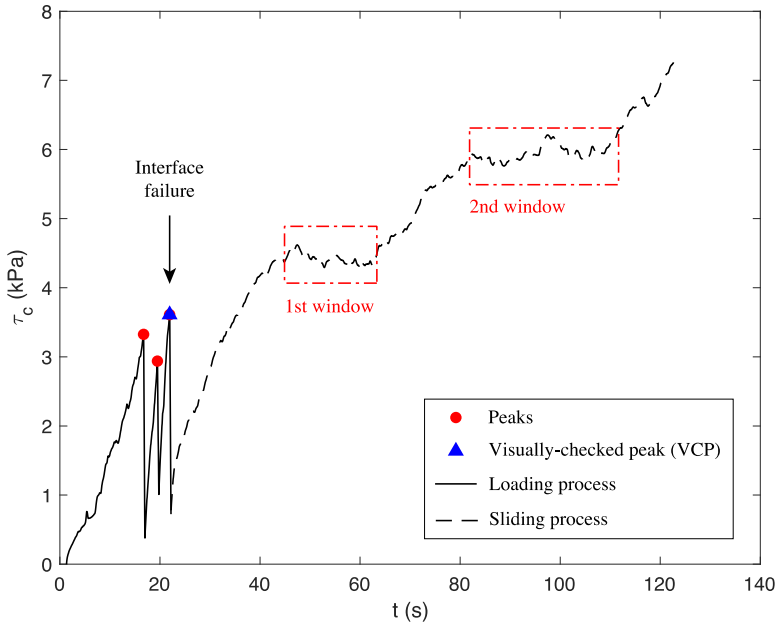

Figure 5 Example of the typical results for shear tests on snow-mortar interface: loading and sliding processes for the LS-T1 test no.1. The black solid line depicts the behaviour of the interface during the loading process, while the dotted one shows the sliding one. Three peaks are identified with the red dots and the blue triangle. The latter one stands for the visually checked peak (VCP). In the sliding process, the two observation windows are identified by red rectangles. The data obtained for these windows are: for the 1st window, mean normal stress $\bar{\sigma}_1^{\mathrm{LS-T1\_no1}} = 4.34$ kPa, mean shear stress $\bar{\tau}_1^{\mathrm{LS-T1\_no1}} = 4.41$ kPa, window time length $WT_1 = 18.6$ s, standard deviation of the normal stress $SD_\sigma = 0.09$ kPa; for the 2nd window: $\bar{\sigma}_2^{\mathrm{LS-T1\_no1}} = 5.11$ kPa, mean shear stress $\bar{\tau}_2^{\mathrm{LS-T1\_no1}} = 5.94$ kPa, window time length $WT_2 = 29.2$ s, standard deviation of the normal stress $SD_\sigma = 0.06$ kPa.

Table 3 Values of the time at failure and relative horizontal displacement at failure for the four types of specimens LS-T1, LS-T2, SS-T1, and SS-T2. The number of usable samples for each specimen type (n) is reported in the second column. n is the number of test (on a maximum of 9) that were successfully carried out during the experimental campaign.

Specimens	n	Relative horizontal displacement at failure	
		Mean value (mm)	Standard deviation (mm)
LS-T1	6	2.62	1.06
LS-T2	6	1.83	1.29
SS-T1	5	3.46	2.86
SS-T2	5	4.22	1.28

After the first process, the slide occurred at the prescribed displacement rate $\dot{u}$ until the achievement of the maximum horizontal displacement (i.e., 20 mm). However, the normal stress σ_c varied during the sliding process and its standard deviation was greater than 0.4 kPa in 90% of the tested specimens (median value: 0.64 kPa, mean value: 0.61 kPa). Generally, the variability of the normal stress is uniformly distributed over all the specimens. Further, the average values of these standard deviations were computed for each specimen, providing the following results: 0.62, 0.62, 0.65, and 0.61 kPa for LS-T1, LS-T2, SS-T1, and SS-T2, respectively. The results are quite similar, showing that the variability of the normal stress is common for all specimens and does not depend on the sample characteristics.

3.2 Typical results of the snow-mortar shear tests

The variability of the normal stress during the tests caused some modifications also in the output graphics and in the following interpretation of the results. Typically, the output of a direct displacement-controlled shear test for which normal stress is ideally constant and represented by a simple stress path like Figure 6a. In the $\tau - t$ plane a loading process (point 1) and a sliding process with nearly constant τ (point 2) can be easily observed, while, in the $\sigma - \tau$ plane, the behaviour is represented by a vertical spike having the maximum at point 1, generally corresponding to the failure envelope of the interface (orange line in Figure 6a). Otherwise, when the normal stress in not constant in time, the stress path is quite disturbed and deviates from the previous vertical trend because of the variability of σ in time (Figure 6b). Thus, when the normal stress is constant in time, it is not necessary to study the entire stress history but only two points are sufficient to represent the resistance behaviour. On the contrary, when the normal stress varies, the entire stress path is useful to investigate the mutual relationships between normal and shear stresses. In this case, several different behaviours could be observed at different levels of σ, even within a single shear test. For these reasons, in the present work the entire stress path was taken into account to interpret the experimental results.

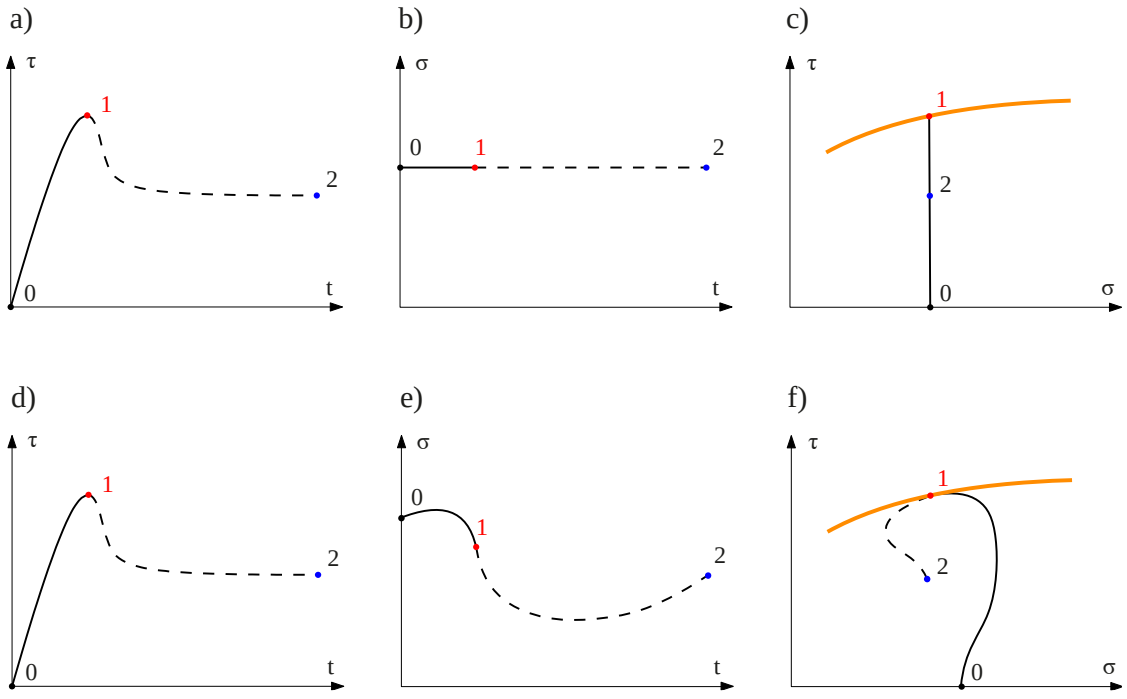

Figure 6 From a) to c), sketches of the typical output of an ideal displacement-controlled direct shear test with constant normal stress σ: a) In the $t-\tau$ plane a clear peak (point 1) can be observed with reference to the failure of the sample. This is followed by a quick decrease of the shear stress, during the sliding process, to a constant value (point 2); b) All processes occur at constant normal stress; c) The stress path $\sigma-\tau$ is a vertical spike reaching the failure envelope (orange line). Notice that the sliding behaviour (dashed line) from point 1 to 2 is hidden by the 0-1 segment. From d) to f), sketches of the typical output of a displacement-controlled direct shear test with variable σ: d) In the $t-\tau$ plane the shape of the curve does not change considerably; e) The variability of the normal stress over time varies with sinusoidal-like shape; f) The stress path $\sigma-\tau$ follows the variability of normal stress in time.

3.3 Operations on the corrected data

Starting from the data corrected following the procedure reported in Sect. 2.4 and considering the main results, the following framework was adopted for the interpretation of the measurements. The data were sorted into the four specimen types (i.e., nine samples for each specimen) previously defined in Sect. 2.3. Within each specimen type a different procedure was applied for loading and sliding processes.

3.3.1 Loading process

In the loading process, the two corrected stresses were plotted with respect to time. For each test i, a certain number j of peaks was identified in the $\tau-t$ plane by using a specifically developed automatic MATLAB script. Then, the peak shear stresses ($\tau_{p,j}^{i}$) and the correspondent peak normal stresses ($\sigma_{p,j}^{i}$) were identified. As an example, the peaks related to the first LS-T1 test are highlighted in Figure 5. The behaviour of the

specimen at any peak condition was checked against the video recording of the event to get further information on the nature of the observed phenomenon, particularly to verify if the loss of strength could be related to the detachment of the snow layer from the mortar surface and the beginning of the sliding process. To this purpose, a Digital Image Correlation (DIC) analysis was performed on the relevant video frames. These peaks, named Visually Checked Peaks (VCP in the following), allowed identification of a single pair of peak stresses for each test: σ_{VCP}^{i}, and τ_{VCP}^{i}. The values of these loading stresses (i.e., stresses at failure) for all tests can be found in Appendix A. These stresses are the only ones that are surely related to the detachment of the snow layer from the mortar (i.e., the failure of the interface). The other peaks may refer to other, unobservable, phenomena such as: fracture of the snow layer, lateral compression of the sample, failures on the snow-mortar interface that could not directly be observed by the video camera, etc. Thus, only VCPs will be taken into account to discuss our experimental results. Finally, for each specimen, the $\sigma_{VCP}^{i} - \tau_{VCP}^{i}$ pairs were fitted by using the following two linear equations, in order to identify the best fitting law:

$$\tau = a\sigma + b \qquad (4_i)$$

$$\tau = a\sigma \qquad (4_{ii})$$

where a and b are two fitting parameters, which were determined with the Nonlinear Least Squares (NLS) method implemented in a MATLAB script (see Sect. 4). The results of the fitting operations for the loading process are reported in Table 4. It can be seen that the values of a and b are comparable between the two proposed fitting laws because of the small values assumed by parameter b in most cases. The one-parameter values derived from Eqn. (4_{ii}) seem more reliable than those obtained via the two-parameters Eqn. (4_i). This is related to two main reasons: i) the one-parameter law provided the highest coefficients of determination (R^2) for all the specimens (especially for SS-T1 specimens), ii) in case of SS-T1 specimens, the two-parameters law resulted in almost nil R^2 because of the low reliability of VCPs data. The results of SS-T1 specimens were compromised by the partial collapse of the snow layer that occurs at the beginning of some tests (especially for low normal stresses). With the aim to partially solve the limitation of SS-T1 data, all the available peaks were considered in the fitting process through the one-parameter law. Finally, the italicized values (i.e., one-parameter values) in Table 4 are those selected to characterize the interface strength (see Sect. 4).

Table 4 Fitting parameters obtained with Eqns. (4_i) and (4_{ii}) for all specimen types during the loading process. All the values were computed on the basis of VCPs except for the star value (SS-T1 type) where the fitting operation was carried out on the basis of all the visualized peaks, in order to have more data. The values highlighted in italics are those selected to characterize the interface strength.

Specimens	Eqn. (4_i) – two-parameters			Eqn. (4_{ii}) – one-parameter	
	a (-)	b (kPa)	R^2 (-)	a (-)	R^2 (-)
LS-T1	0.947	-0.13	0.761	*0.927*	*0.760*
LS-T2	0.807	0.18	0.545	*0.833*	*0.544*
SS-T1	-0.051	4.60	0.020	*0.622* (*)	*0.724* (*)
SS-T2	0.523	0.21	0.685	*0.561*	*0.681*

3.3.2 Sliding process

For the sliding process, a different approach was adopted. First of all, for each test, the sliding process data was isolated from the rest of the data. Then, two temporal windows were identified for each test by observing the evolution of the two stress components over time. The windows had to satisfy three requirements: i) within the windows, the sliding of the snow layer has to be evident, ii) each window has to span more than 10 s ($WT > 10$ s) in order to be representative of the sliding process, and iii) the standard deviation of the normal stress (SD_σ) has to be smaller than 0.1 kPa, to reduce the variability of the data. These conditions are needed to identify portions of sliding process in which the normal stress remains almost constant for a sufficient period of time. Then, for the i-th test and the j-th window (with $j = 1,2$), the average values of the normal stress ($\bar{\sigma}_j^i$) and of the shear stress ($\bar{\tau}_j^i$) were computed (Figure 5). The values of these "sliding stresses" for all tests can be found in Appendix A. Finally, the so obtained two $\bar{\sigma}_j^i - \bar{\tau}_j^i$ pairs were linearly fitted following the Eqns. (4_i) and (4_{ii}). Also, in this case, the above-mentioned procedure was applied to all specimens and the highest coefficients of determination are those obtained with the two-parameters fitting described by Eqn. (4_i). The results of the fitting operations for the sliding process are reported in Table 5 where the italicized values (i.e., two-parameters values) are those selected to characterize the interface strength (see Sect. 4).

Table 5 Fitting parameters obtained with Eqns. (4_i) and (4_{ii}) for all the specimens during the sliding process. The values highlighted in italics are those selected to characterize the interface strength.

Specimens	Eqn. (4_i) – two-parameters			Eqn. (4_{ii}) – one-parameter	
	a (-)	b (kPa)	R^2 (-)	a (-)	R^2 (-)
LS-T1	*0.429*	*2.10*	*0.929*	0.70	0.516
LS-T2	*0.589*	*1.05*	*0.778*	0.73	0.733
SS-T1	*0.412*	*0.18*	*0.874*	0.43	0.872
SS-T2	*0.534*	*0.90*	*0.893*	0.66	0.841

3.4 Image analysis

As it was previously described, all tests were filmed with a digital video camera through the dedicated window on the external side of the shear box. These footages allowed to follow and compare the sensor data with the actual phenomena occurring to each sample.

With reference to only the sliding process the Particle Image Velocimetry (PIV, hereafter) was applied to some frames to better visualize the motion field during the test. The results do not show significant differences among the four groups of specimens. Therefore, for the sake of clarity, we depict the main results obtained by the PIV technique with reference to SS-T1 test no. 4 (Figure 7). In this case, we performed the PIV analysis on the basis of 20 frames taken at 0.5 s from each other, and between 43.5 and 53 s after the beginning of the test (i.e., 33.5 and 43 s after the failure occurrence). In Figure 7, three images are reported as example, caught at 43.5, 50, and 53 s, respectively. A rectangular (27.7 × 27.1 mm) region of interest (ROI, hereafter) was determined and the PIV analysis was carried out inside this region with the open source MATLAB app PIVlab (Thielicke and Stamhuis, 2014). It can be seen that, during the sliding process, the horizontal component of the velocity ($\dot{u}$) is the same in all snow parts of the sample. The absolute value of the mean value of $\dot{u}$ is about $1.6 \cdot 10^{-5}$ m s^{-1}, which is substantially equivalent to the imposed displacement rate (i.e., 10 mm min^{-1}). Thus, one can conclude that during the test, the shear action was efficiently transmitted from the shear box to the tested specimen. The transition between these velocity values and null values (i.e., the mortar half of the specimen) happens in a very thin and horizontal band at the contact between snow and mortar, having a thickness of about 0.4 mm on average. Figure 7 also shows that in this thin layer non-null values of vorticity are present where a sort of circular movement (whirl) of snow crystals can be observed. In other zones (such as on the right part of the image at 50 s frame), this band deviates from its typical horizontal condition. This is due to some snow grains that instantaneously stop and are bypassed by others that continue their horizontal movement. A zoomed image of the contact zone is provided in Figure 8. Here, it can be observed that the instantaneous adhesion of portions of the snow layer to the underneath mortar substrate causes whirl movements (or vortices) in the neighbour snow particles (Figure 8e). A similar pattern of behaviour has been observed in other studies relating to both snow (De Biagi et al., 2019b) and granular media in general (Tordesillas et al., 2016).

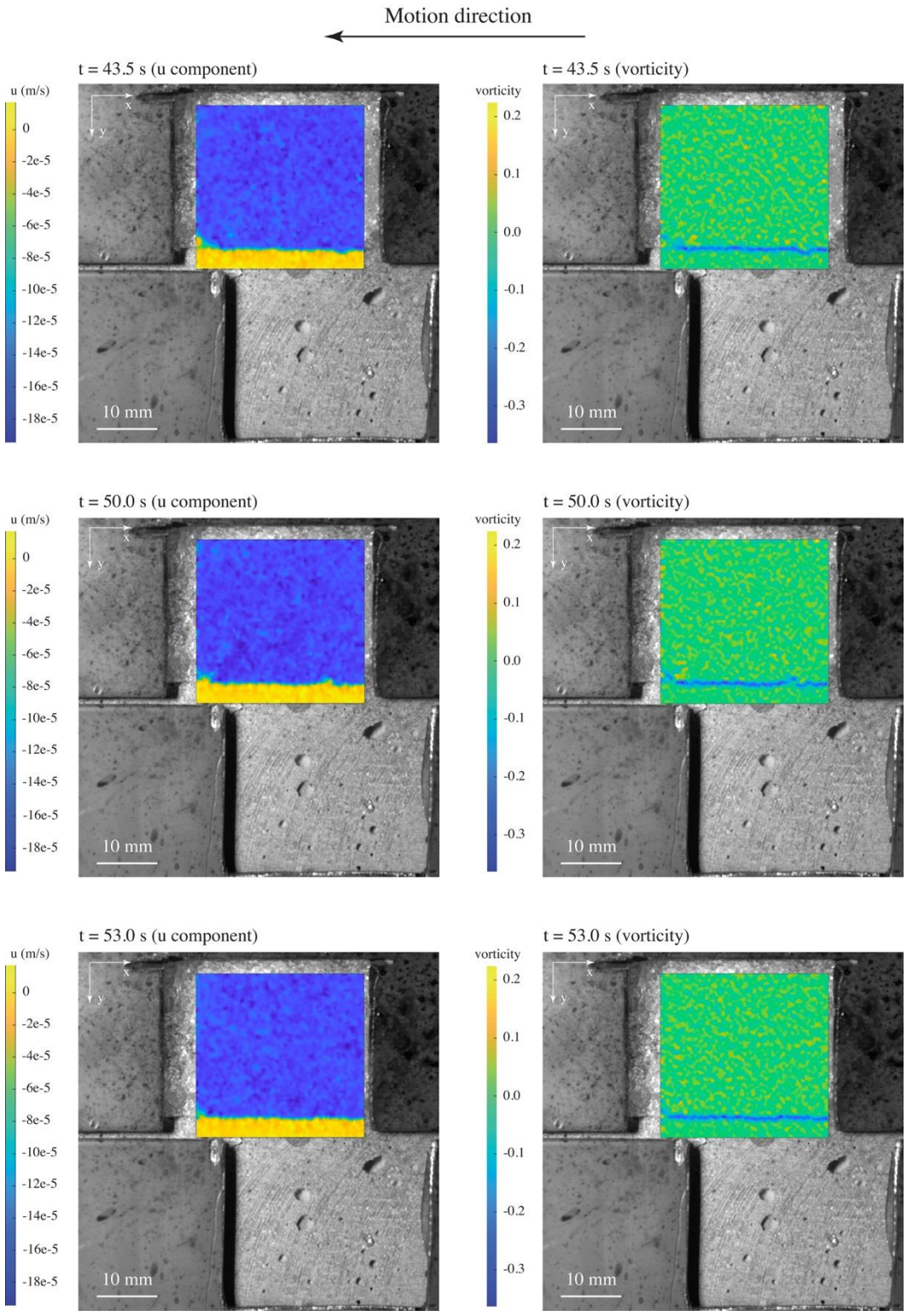

Figure 7 Frames of the sliding process of SS-T1 test no. 4 between 43.5 and 53 s. The horizontal component of velocity is reported on the left, while the vorticity can be seen on the right.

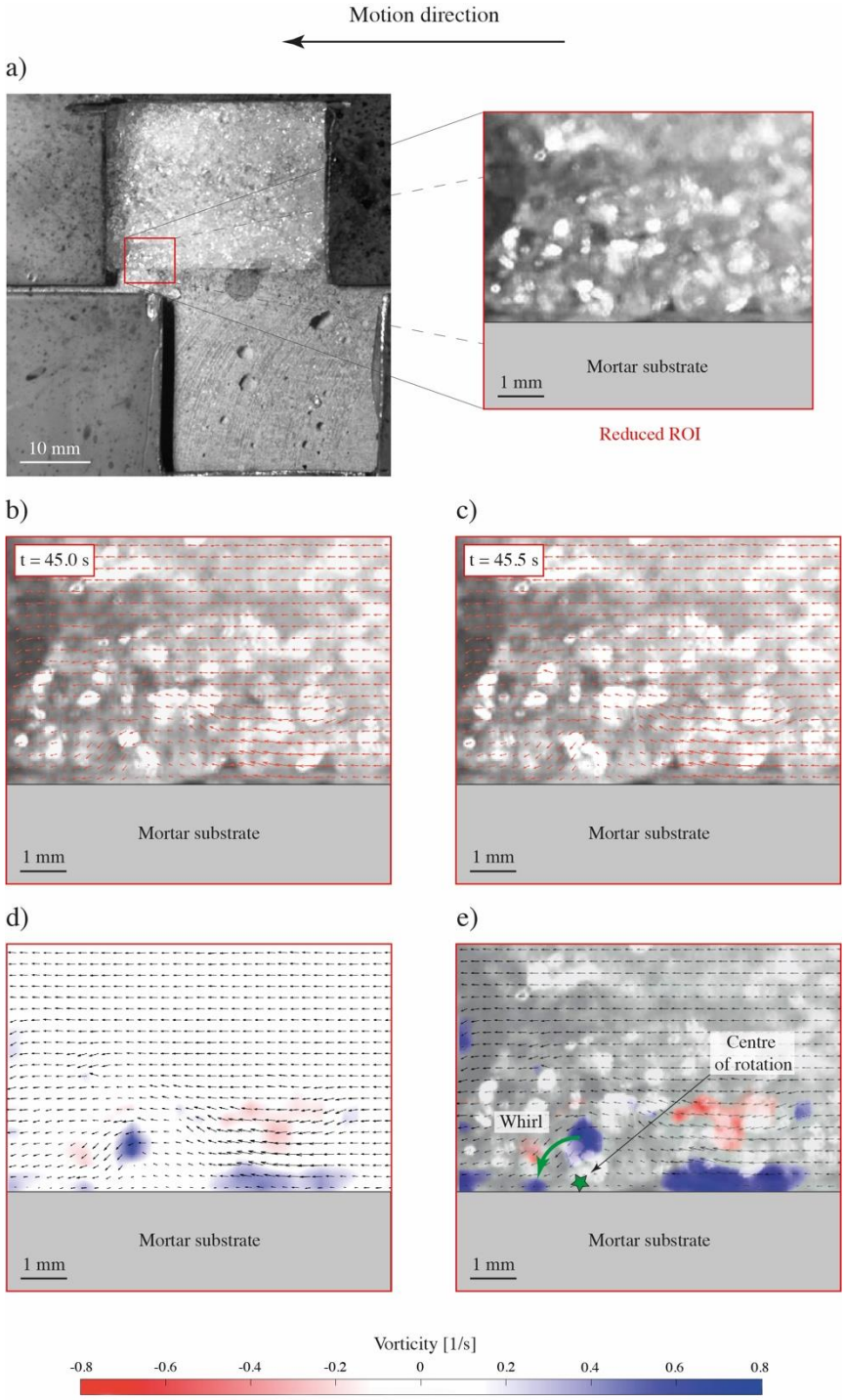

455

456 **Figure 8** Zoomed image of the snow layer in contact with the mortar substrate (SS-T1 test no. 4): a)
457 Location of the reduced ROI (red rectangle) within the video frame; b) Surface pattern of snow and velocity
458 field (red arrows) at t = 45.0 s (from the beginning of the test); c) Surface pattern of snow and velocity field
459 (red arrows) at t = 45.5 s; d) Map of the vorticity, the red and blue areas pointed to the zones with clockwise
460 and counterclockwise whirls, respectively, while the white areas represent the zones with zero vorticity; e)
461 Map of the vorticity with snow pattern in background. The chromatic scale was emphasized to better
462 identify the different zones with respect to the background. The green arrow identifies a whirl movement
463 originated by snow particles that bypass a zone where the snow adheres to the underneath mortar substrate.
464 Inside this "bridge" zone the center of rotation can be clearly observed (green star).

4 Discussion

To evaluate the influence of the normal stress on both sintering time and temperature conditions, we assume that the interface shear strength is governed by the Mohr-Coulomb criterion:

$$\tau_{l,s} = \tan\phi\, \sigma_{l,s} + c \tag{5}$$

where ϕ is the equivalent friction angle of the interface, c is the parameter usually called "cohesion" in the geotechnical literature, and subscripts l and s stand for loading and sliding processes, respectively. The same model was applied for both processes. Within the international scientific literature, the Mohr-Coulomb law is largely adopted in the fields of geotechnical and structural engineering for many different applications (e.g., soil and rock mechanics). Also, for snow mechanics the model is widely used to characterize the failure criteria of snow samples in many experimental activities (De Biagi et al., 2019b; Matsushita et al., 2012; Podolskiy et al., 2014). Thus, the choice of this type of model seems to be reasonable, especially in case of first experimental results as these.

The estimation of the two parameters (ϕ and c) of the Mohr-Coulomb law was carried out starting from the coefficients a and b contained in Tables 4 and 5. These coefficients are linked to ϕ and c as follows:

$$\phi = \tan^{-1} a \tag{6$_i$}$$

$$c = b \tag{6$_{ii}$}$$

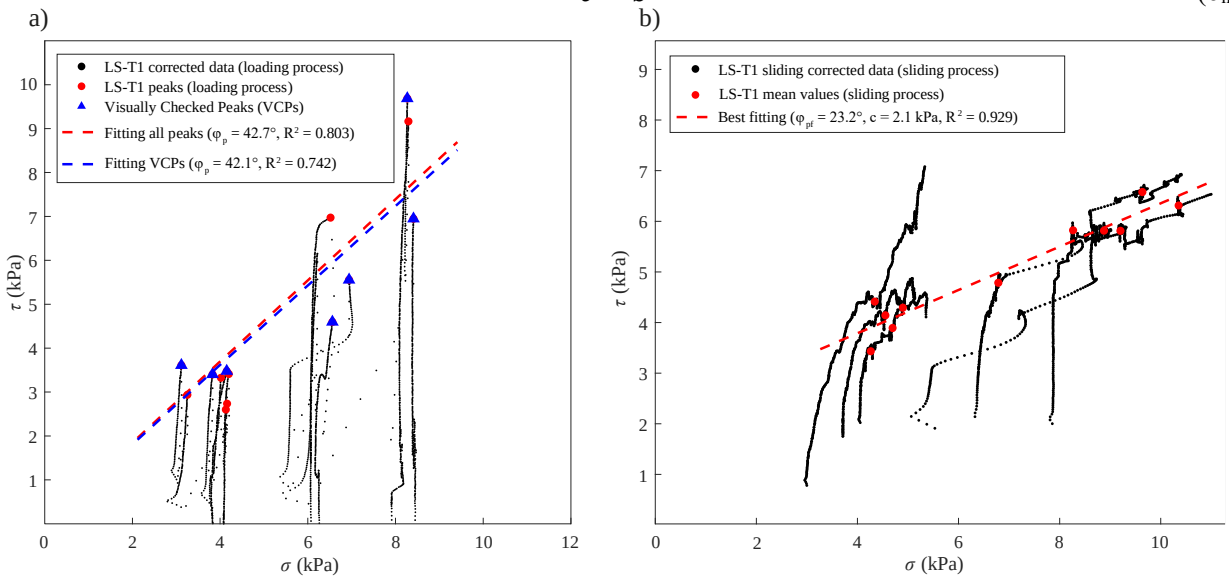

Figure 9 a) Example of the interpretation for the loading process of LS-T1 specimens with both one-parameter fitting laws; b) Interpretation of the sliding process for LS-T1 specimens with the two-parameters fitting law. Red points refer to the mean values computed for the two observation windows.

The best estimation of the Mohr-Coulomb parameters can be found in Table 6, while an example of the fitting results for both loading and sliding process is reported in Figure 9 for the case of LS-T1 specimens. One can observe that a one-parameter fitting law was used for the loading process while a two-parameter expression was adopted for the sliding one. Referring to loading process, the two possible fitting laws provide essentially the same results, and, in most cases, the intercept calculated for the two-parameter law, i.e., the value of shear strength for zero normal stress on the interface, was found to be very close to zero and consequently a one-coefficient relation was adopted ($c \approx 0$ kPa).

Otherwise, during the sliding process, a non-zero intercept (c) was generally found, and a two-parameters law was used. It can be noted that here c is devoid of a well-defined physical meaning because during sliding process the behaviour of snow-mortar interface is strictly frictional. Therefore, c is not a cohesion parameter and assumes only a purely mathematical significance (i.e., an intercept). The existence of c originates from the experimental conditions adopted in this work. The entire experimental activity was indeed carried out within a limited range of normal stresses, i.e., between 2 and 10 kPa. Thus, no further conclusions can be drawn outside this range and the linear interpolation is only reliable inside it. For lower normal stresses, it is very likely that the behaviour of snow-mortar interface is non-linear, and nil shear stress could be found at $\sigma_n = 0$ kPa. In this work, the best possible (two-parameters) linearization, in the investigated pressure range, of the supposed non-linear interface behaviour was used. On the contrary, the slope angle ϕ assumes the meaning of a friction angle for the snow-mortar interface and its tangent can be interpreted as its friction coefficient for the sliding process.

Table 6 Final values adopted for the estimation of the Mohr-Coulomb parameters for both loading and sliding processes. The last column refers to the friction coefficients evaluated as $\mu_{l,s} = \tan \phi_{l,s}$.

Specimen type	Loading process			Sliding process		
	ϕ_l (°)	c (kPa)	μ_l (-)	ϕ_s (°)	c (kPa)	μ_s (-)
LS-T1	42.8	0.00	0.927	23.2	2.10	0.429
LS-T2	39.8	0.00	0.833	30.5	1.05	0.589
SS-T1	31.9	0.00	0.724	22.4	0.18	0.412
SS-T2	29.3	0.00	0.561	28.1	0.90	0.534

Despite the complex correction and interpretation procedures, the final outputs of the experimental activity provide some interesting results. For the loading process, we conclude that the effect of sintering time on

505 friction angle is more relevant than that of temperature. In Table 6 a difference in ϕ of about 10° can be
506 observed passing from long sintering to short sintering times, while only 2° distinguishes between T1 and T2.
507 As a general comment, we state that longer sintering times and lower temperatures induce higher friction
508 angles. Our initial interpretation of the observed behaviour is that the larger ϕ-values observed in the first
509 phase is related to the surface adhesion acting on the snow-mortar interface (Mellor, 1975). In fact, a possible
510 explanation is that the phenomenon occurs if water particles (or ice particles) are present on the mortar surface.
511 Large sintering times promote the formation of "bridges" (or surface bonds) between the snow layer and the
512 underneath rigid material, enhancing at the same time the external action needed to break them (Jelle, 2013;
513 Jellinek, 1960). These bridges are actually adhesive bonds in which adhesive forces of electromagnetic or
514 electrostatic nature act. The adhesive forces are responsible for the complex behaviour of snow on stiffer
515 material that can potentially originate a high shear resistance, such as a hard snow layer firmly adhering to a
516 pseudo-vertical surface (rock, glass, etc.). Evidence of this type of adhesion between cold snow and a solid
517 surface can be found in some literature works (Heil et al., 2020; Inoue and Honda, 1955; Jelle, 2013; Jellinek,
518 1960; Mellor, 1975). In the second process, on the contrary, an opposite trend emerges: it seems that the
519 influence of temperature on shear strength is more relevant than the one of the sintering times. Smaller friction
520 angles can be related to lower temperatures, while higher friction is promoted in warmer snowpack. With equal
521 temperature, longer sintering time increases of only 0.8° and 2.4° the friction angle, with reference to T1 and
522 T2, respectively.

523 Despite few works on snow-solid interface strength exist, it is possible to relate our findings with literature
524 data. For instance, Jelle (2013) carried out a series of tilt tests with snow layers deposited on different types of
525 substrate. He found that in case of snow-concrete the detachment of snow occurred with a tilt-angle of 31°
526 which corresponds to a 0.6 static friction coefficient. This value is comparable with our loading values that are
527 ranging between 0.561 and 0.927. According to the general knowledge of materials behaviour, friction should
528 be also dependent on the displacement rate (Persson, 2013). In particular, for snow mechanics, this dependence
529 is extremely important and can result in the main triggering factor for avalanche release (Puzrin et al., 2019).
530 The experimental activity described in this paper was carried out at a given displacement rate (i.e., $\dot{u} = 10$
531 mm min^{-1}). Nevertheless, it is possible to relate the obtained friction coefficients to some data reported in the
532 literature. For instance, Makkonen and Tikanmäki (2014) provided a series of friction coefficients determined

on the basis of tests on ice-ice, rubber-ice, steel-ice, and PMMA-ice interfaces. The tests had been conducted at a temperature of -10 °C and different velocities were considered, ranging from 10^{-6} to 10^{2} m s^{-1}. It was found that our results, obtained for a velocity of 10 mm min^{-1} = 1.67 · 10^{-4} m s^{-1}, are consistent with the results of these literature data. For ice-ice, ice-steel and ice-PMMA interfaces, the paper gives values in the range from 0.35 to 0.55, which are comparable with our sliding values that are ranging between 0.429 and 0.589. Unfortunately, the above-mentioned friction coefficients were provided only for the cited materials and only for ice which has characteristics different from seasonal snow.

5 Conclusions

In this study, we quantified the frictional behaviour of a snow layer at contact with a rigid substrate (mortar block) on the basis of a laboratory experimental campaign carried out with a portable shear test device. We performed 36 direct shear tests on artificially assembled interface specimens made by two superimposed halves: a bottom mortar block and an upper snow layer. The tests were performed at different temperatures (i.e., T1 = -10 °C and T2 = -5 °C) and sintering times (i.e., long sintering: LS = 20 hours, and short sintering: SS = 20 minutes), to investigate the influence of these two parameters on the shear strength of the interface.

We also developed a methodology of analysis that provides some preliminary and promising results despite the limitations affecting the adopted testing system (i.e., variability of normal stresses, noise of the signals, etc.). In particular, the following key points arise from the present work:

- The results represent the first step in the direction of a better comprehension of many problems relating to the shear strength of a cold snow layer in contact with solids, a study still lacking of sufficient references within the international scientific literature.
- The shear strength of the tested interface can be easily interpreted by the Mohr-Coulomb criterion which allows the understanding of the two opposite behaviours in loading and sliding processes.
- The Mohr-Coulomb parameters show a clear dependence on both sintering time and temperature. In particular, two opposite trends can be observed: during the loading process, for both sintering times, the friction coefficient decreases when the room temperature increases; otherwise, in the sliding process, friction coefficient and room temperature grow together.

- The experimental results show the formation of a surface adhesion acting between the mortar slab and the snow layer, which is confirmed by several studies (Heil et al., 2020; Inoue and Honda, 1955; Jelle, 2013; Jellinek, 1960; Mellor, 1975). Exceeding this adhesion threshold causes the failure of the interface and the following relative sliding between the two halves of the specimen that essentially act as rigid bodies.

Further improvements of the shear apparatus could solve the issues affecting the present experimental activity, also confirming the interpretation of the results described here and improving them. In particular, some future modifications include:

- The shear device can be improved in many aspects. For instance, the variability of the normal stress can be fixed by introducing a larger air chamber directly inside the shear box which is able to maintain the pressure constant, or designing a new pneumatic system based, for example, on liquid medium instead of air.
- With reference to the topic of this research, one of the most interesting aspects to be studied in the future is the effect of temperatures close to the melting point of snow that could better represent the conditions of a natural ground-snow interface when the temperature is kept constant by the insulating effect of the snow cover itself. Another item, strictly related to the latter, could be the investigation of the role of liquid water content at the snow-mortar interface on both loading and sliding processes. Also, other types of snow crystals and grains, even harvested on-site, can be used to perform more reliable analyses. Finally, the only two-dimensional image analysis carried out in this work is not able to provide sufficiently reliable results that can be used to derive more general conclusion on the entire surface contact. Further improvements could overcome these limits by implementing transparent sides for the shear box or using other non-invasive techniques, such as acoustic emissions.

Declaration of Competing Interests

The authors declare that they have no known competing financial interests or personal relationships that could have appeared to influence the work reported in this paper.

Author Contribution

Gianmarco Vallero: Conceptualization, methodology, formal analysis, writing – original data, writing – review & editing, visualization. Monica Barbero: investigation, data curation, writing – review & editing, supervision. Fabrizio Barpi: investigation, data curation, writing – review & editing, supervision. Mauro Borri-Brunetto: investigation, data curation, writing – review & editing, supervision. Valerio De Biagi: writing – review & editing, supervision. Yoichi Ito: investigation, data curation, writing – review & editing. Satoru Yamaguchi: investigation, data curation, writing – review & editing. All authors have read and agreed to the published version of the manuscript.

Funding

This research did not receive any specific grant from funding agencies in the public, commercial, or not-for-profit sectors.

Acknowledgements

Some of the concepts contained in this work had been firstly put forward in the Master's thesis in Civil Engineering (Politecnico di Torino) of S. Corrao, advised by five of the authors (Borri-Brunetto, Barbero, Barpi, De Biagi and Vallero), whose early contribution is gratefully acknowledged.

Appendices

Appendix A

Table A.1 Corrected data for both loading and sliding processes and for all the tested specimens. σ_{VCP} and τ_{VCP} represent the stress components for all the VCPs. $\bar{\sigma}_1$ and $\bar{\tau}_1$ are the mean value within the first window of the sliding process, while $\bar{\sigma}_2$ and $\bar{\tau}_2$ are referred to the second window. Notes: 1) missing data; 2) test not considered for both loading and sliding analyses because of the global collapse of the specimen that compromise the test output; 3) test not considered because the motor does not reach the required displacement rate; 4) test in which only the loading process was considered because during the sliding process the relative movement between the two halves of the specimen was compromised by the collapse of the sample; 5) test in which only the sliding process was considered because during the loading process the detachment of the snow layer is not clear in the video recording of the test.

Test extended name	Loading process			Sliding process				Notes
	u at failure (mm)	σ_{VCP} (kPa)	τ_{VCP} (kPa)	$\bar{\sigma}_1$ (kPa)	$\bar{\tau}_1$ (kPa)	$\bar{\sigma}_2$ (kPa)	$\bar{\tau}_2$ (kPa)	
LS-T1 test no. 1	3.38	3.12	3.61	4.34	4.41	5.11	5.95	
LS-T1 test no. 2	3.02	4.15	3.48	4.26	3.43	4.69	3.89	
LS-T1 test no. 3	2.00	3.83	3.40	4.55	4.14	4.90	4.29	
LS-T1 test no. 4	-	-	-	-	-	-	-	3)
LS-T1 test no. 5	4.15	6.56	4.60	6.79	4.78	8.27	5.82	
LS-T1 test no. 6	-	-	-	-	-	-	-	2)
LS-T1 test no. 7	2.50	8.27	9.69	8.88	5.81	9.64	6.58	
LS-T1 test no. 8	3.61	8.41	6.95	9.20	5.81	10.35	6.31	
LS-T1 test no. 9	-	-	-	-	-	-	-	
LS-T2 test no. 1	1.16	4.14	4.19	5.29	4.74	6.09	5.17	
LS-T2 test no. 2	-	-	-	-	-	-	-	1)
LS-T2 test no. 3	1.72	5.10	4.46	5.50	3.82	5.73	3.87	
LS-T2 test no. 4	1.04	5.98	3.46	7.01	5.36	7.52	5.50	
LS-T2 test no. 5	0.70	5.94	3.92	7.66	6.28	8.60	6.46	
LS-T2 test no. 6	4.87	6.15	6.45	6.66	4.45	7.80	5.07	
LS-T2 test no. 7	-	-	-	-	-	-	-	3)
LS-T2 test no. 8	1.76	8.55	7.50	9.27	6.21	10.07	6.96	
LS-T2 test no. 9	-	-	-	-	-	-	-	2)
SS-T1 test no. 1	-	-	-	-	-	-	-	1)
SS-T1 test no. 2	-	-	-	-	-	-	-	2)
SS-T1 test no. 3	3.30	4.26	4.26	-	-	-	-	4)
SS-T1 test no. 4	0.77	5.96	4.35	6.63	2.85	7.46	3.03	
SS-T1 test no. 5	0.50	6.12	4.78	6.49	2.75	7.46	3.64	
SS-T1 test no. 6	4.38	6.68	3.85	7.19	4.78	7.58	5.88	
SS-T1 test no. 7	-	-	-	8.96	3.97	10.02	4.51	5)
SS-T1 test no. 8	-	-	-	-	-	-	-	2)
SS-T1 test no. 9	-	-	-	9.04	3.91	10.06	4.02	5)
SS-T2 test no. 1	2.84	4.56	3.14	4.79	3.46	5.47	4.03	
SS-T2 test no. 2	3.49	4.48	2.78	5.71	4.21	6.11	4.63	
SS-T2 test no. 3	6.47	4.13	1.69	5.33	3.52	5.63	3.90	
SS-T2 test no. 4	4.71	6.70	3.88	6.86	4.39	8.08	4.85	
SS-T2 test no. 5	3.58	7.00	3.58	7.17	4.45	7.76	4.71	
SS-T2 test no. 6	-	-	-	-	-	-	-	2)
SS-T2 test no. 7	-	-	-	8.75	5.58	9.94	6.67	5)
SS-T2 test no. 8	-	-	-	-	-	-	-	2)
SS-T2 test no. 9	-	-	-	-	-	-	-	2)

612 **References**

613 Abele, G., 1963. A correlation of unconfined compressive strength and ram hardness of processed snow.
614 CRREL Tech. Rep. 14.

615 Ancey, C., Bain, V., 2015. Dynamics of glide avalanches and snow gliding. Rev. Geophys. 53, 745–784.
616 https://doi.org/10.1002/2015RG000491

617 Barbero, M., Barpi, F., Borri-Brunetto, M., Pallara, O., 2016. An apparatus for in situ direct shear tests on
618 snow. Exp. Tech. 40, 149–158.

619 Bartko, M., Baskaran, A., 2018. Snow Friction Coefficient for Commercial Roofing Materials. J. Cold Reg.
620 Eng. 32, 06017005. https://doi.org/10.1061/(asce)cr.1943-5495.0000146

621 Casassa, G., Narita, H., Maeno, N., 1991. Shear cell experiments of snow and ice friction. J. Appl. Phys. 69,
622 3745–3756. https://doi.org/10.1063/1.348469

623 Casassa, G., Narita, H., Maeno, N., 1989. Measurements of friction coefficients of snow blocks. Ann.
624 Glaciol. 13, 40–44. https://doi.org/10.1017/s0260305500007618

625 Colbeck, S.C., 1994. A review of the friction of snow skis. J. Sports Sci. 12, 285–295.

626 Conway, H., Abrahamson., J., 1984. Snow stability index. J. Glaciol. 30, 321–327.

627 De Biagi, V., Barbero, M., Barpi, F., Borri-Brunetto, M., Pallara, O., 2019a. Improvements on an existing
628 testing device to study post-peak shear behaviour of snow. Geophys. Res. Abstr. 21.

629 De Biagi, V., Barbero, M., Barpi, F., Borri-Brunetto, M., Podolskiy, E., 2019b. Failure mechanics of snow
630 layers through image analysis. Eur. J. Mech. A/Solids 74, 26–33.
631 https://doi.org/10.1016/j.euromechsol.2018.10.018

632 Fierz, C.., Armstrong, R.L.., Durand, Y.., Etchevers, P.., Greene, E.., McClung, D.M.., Nishimura, K..,
633 Satyawali, P.K.., Sokratov, S.A.., 2009. The international classification for seasonal snow on the
634 ground.

635 Gauthier, D., Brown, C., Jamieson, B., 2010. Modeling strength and stability in storm snow for slab

avalanche forecasting. Cold Reg. Sci. Technol. 62, 107–118. https://doi.org/10.1016/j.coldregions.2010.04.004

Gleason, J., 2002. Preliminary results of snow surface friction coefficient measurements, in: International Snow Science Workshop. pp. 523–527.

Heil, J., Mohammadian, B., Sarayloo, M., Bruns, K., Sojoudi, H., 2020. Relationships between surface properties and snow adhesion and its shedding mechanisms. Appl. Sci. 10. https://doi.org/10.3390/APP10165407

Höller, P., Fromm, R., 2010. Quantification of the hand hardness test. Ann. Glaciol. 51, 39–44. https://doi.org/10.3189/172756410791386454

Inoue, R., Honda, T., 1955. Mesurement of Adhesion between Snow and a Solid Surface. J. Japanese Soc. Snow Ice 17, 18–20.

Jelle, B.P., 2013. The challenge of removing snow downfall on photovoltaic solar cell roofs in order to maximize solar energy efficiency - Research opportunities for the future. Energy Build. 67, 334–351. https://doi.org/10.1016/j.enbuild.2013.08.010

Jellinek, H.H.G., 1960. Adhesive Properties of Ice, Part II. Wilmette, Illinois.

Kietzig, A.M., Hatzikiriakos, S.G., Englezos, P., 2010. Physics of ice friction. J. Appl. Phys. 107. https://doi.org/10.1063/1.3340792

Kietzig, A.M., Hatzikiriakos, S.G., Englezos, P., 2009. Ice friction: The effects of surface roughness, structure, and hydrophobicity. J. Appl. Phys. 106. https://doi.org/10.1063/1.3173346

Makkonen, L., Tikanmäki, M., 2014. Modeling the friction of ice. Cold Reg. Sci. Technol. 102, 84–93. https://doi.org/10.1016/j.coldregions.2014.03.002

Matsushita, H., Matsuzawa, M., Abe, O., 2012. The influences of temperature and normal load on the shear strength of snow consisting of precipitation particles. Ann. Glaciol. 53, 31–38. https://doi.org/10.3189/2012AoG61A022

McCallum, A., 2014. Cone Penetration Testing (CPT): A valuable tool for investigating polar snow. J.

661 Hydrol. New Zeal. 52, 97–113.

662 McCallum, A., White, G.W., 2016. Engineered Pavement of Snow and Ice, in: 8th International Conference
663 on Snow Engineering. Centre Scientifique et Technique du Bâtiment (CSTB), Nantes (France).

664 McCallum, A., Wiegand, A., 2018. Simple Method for Estimating Snow Strength Using CPT Sleeve Friction
665 Data. J. Cold Reg. Eng. 32, 04018013. https://doi.org/10.1061/(asce)cr.1943-5495.0000170

666 McClung, D., Schaerer, P.A., 2006. The avalanche handbook. Mountaineers Books.
667 https://doi.org/10.5860/choice.31-3797

668 McClung, D.M., 1979. Shear fracture precipitated by strain softening as a mechanism of dry slab avalanche
669 release. J. Geophys. Res. Solid Earth 84, 3519–3526. https://doi.org/10.1029/JB084iB07p03519

670 McClung, D.M., 1977. Direct Simple Shear Tests on Snow and Their Relation to slab avalanche formation.
671 J. Glaciol. 19, 101–109.

672 Mede, T., Chambon, G., Hagenmuller, P., Nicot, F., 2018. Snow Failure Modes Under Mixed Loading.
673 Geophys. Res. Lett. 45, 13,351-13,358. https://doi.org/10.1029/2018GL080637

674 Mellor, M., 1975. A review of basic snow mechanics. Snow Mech. (Proceedings Grindelwald Symp. April
675 1974), IAHS Publ.\ no.\ 114 251–291.

676 Mitterer, C., Schweizer, J., 2012. Towards a better understanding of glide-snow avalanche formation. Int.
677 Snow Sci. Work. 610–616.

678 Persson, B., 2013. Sliding friction: physical principles and applications. Springer-Verlag Berlin Heidelberg.
679 https://doi.org/10.1007/978-3-662-04283-0

680 Podolskiy, E.A., Barbero, M., Barpi, F., Chambon, G., Borri-Brunetto, M., Pallara, O., Frigo, B., Chiaia, B.,
681 Naaim, M., 2014. Healing of snow surface-to-surface contacts by isothermal sintering. Cryosphere 8,
682 1651–1659. https://doi.org/10.5194/tc-8-1651-2014

683 Portnoff, M.R., 1980. Time-Frequency Representation of Digital Signals and Systems Based on Short-Time
684 Fourier Analysis. IEEE Trans. Acoust. Speech, Signal Process. 28, 55–69.

685 Puzrin, A.M., Faug, T., Einav, I., 2019. The mechanism of delayed release in earthquake-induced
686 avalanches. Proc. R. Soc. A Math. Phys. Eng. Sci. 475. https://doi.org/10.1098/rspa.2019.0092

687 Reiweger, I., Ernst, R., Schweizer, J., Dual, J., 2009. Force-controlled shear experiments with snow samples.
688 ISSW 09 - Int. Snow Sci. Work. Proc. 120–123.

689 Reiweger, I., Schweizer, J., Ernst, R., Dual, J., 2010. Load-controlled test apparatus for snow. Cold Reg. Sci.
690 Technol. 62, 119–125. https://doi.org/10.1016/j.coldregions.2010.04.002

691 Schweizer, J., Jamieson, J.B., Schneebeli, M., 2003. Snow avalanche formation. Rev. Geophys. 41.
692 https://doi.org/10.1029/2002RG000123

693 Shapiro, L., Johnson, J., Sturm, M., Blaisdell, G., 1997. Snow Mechanics - Review of the State of
694 Knowledge and Applications.

695 Sugiura, K., Yang, D., Ohata, T., 2011. Rapid change of tundra snow hardness in Alaska. Ann. Glaciol. 52,
696 97–101. https://doi.org/10.3189/172756411797252040

697 Takeuchi, Y., Nohguchi, Y., Kawashima, K., Izumi, K., 1998. Measurement of snow-hardness distribution.
698 Ann. Glaciol. 26, 27–30.

699 Thielicke, W., Stamhuis, E.J., 2014. PIVlab – Towards User-friendly, Affordable and Accurate Digital
700 Particle Image Velocimetry in MATLAB. J. Open Res. Softw. 2. https://doi.org/10.5334/jors.bl

701 Tordesillas, A., Pucilowski, S., Lin, Q., Peters, J.F., Behringer, R.P., 2016. Granular vortices: Identification,
702 characterization and conditions for the localization of deformation. J. Mech. Phys. Solids 90, 215–241.
703 https://doi.org/10.1016/j.jmps.2016.02.032

704 Turner, D., Crozier, P., Reu, P., 2015. Digital Image Correlation Engine.

705 White, G., McCallum, A., 2018. Review of ice and snow runway pavements. Int. J. Pavement Res. Technol.
706 11, 311–320. https://doi.org/10.1016/j.ijprt.2017.11.002

707